

Atomistic mechanisms of phase transitions in all-temperature barocaloric material KPF_6

Jiantao Wang,^{1,2} Yi-Chi Zhang,^{1,2} Yan Liu,^{1,2} Hongkun Deng,^{1,2}
Mingfeng Liu,¹ Yan Sun,¹ Bing Li,¹ Xing-Qiu Chen,^{1,*} and Peitao Liu^{1,†}

¹*Shenyang National Laboratory for Materials Science, Institute of Metal Research,
Chinese Academy of Sciences, 110016 Shenyang, China*

²*School of Materials Science and Engineering, University of Science and Technology of China, 110016 Shenyang, China*

Conventional barocaloric materials typically exhibit limited operating temperature ranges. In contrast, KPF_6 has recently been reported to achieve an exceptional all-temperature barocaloric effect (BCE) via pressure-driven phase transitions. Here, we elucidate the atomistic mechanisms underlying the phase transitions through first-principles calculations and machine-learning potential accelerated molecular dynamics simulations. We identify four distinct phases: the room-temperature cubic (C) plastic crystal characterized by strong fluorine orientational disorder (FOD) and anharmonicity, the intermediate-temperature monoclinic (M-II) phase with decreasing FOD, the low-temperature monoclinic (M-I) phase with suppressed FOD, and the fully ordered rhombohedral (R) phase under pressure. Phonon calculations confirm the dynamic stability of the M-II, M-I, and R phases at 0 K, whereas the C phase requires thermal fluctuations for stabilization. Under pressure, all the C, M-II, and M-I phases transform to the R phase, which are driven by cooperative PF_6 octahedral rotations coupled with lattice modulations. These pressure-induced phase transitions result in persistent isothermal entropy changes across a wide temperature range, thereby explaining the experimentally observed all-temperature BCE in this material. Hybrid functional calculations reveal wide-bandgap insulating behavior across all phases. This work deciphers the interplay between FOD, anharmonicity, and phase transitions in KPF_6 , providing important insights for the design of BCE materials with broad operational temperature spans.

I. INTRODUCTION

Caloric effects, driven by external fields such as magnetic fields [1], electric fields [2], uniaxial stress [3], or hydrostatic pressure [4], present a promising avenue for solid-state refrigeration, offering a sustainable alternative to conventional vapor-compression systems. Among these, the barocaloric effect (BCE)—characterized by isothermal entropy changes or adiabatic temperature changes upon pressure application or removal—stands out due to its universality, scalability, and large thermal responses [4, 5]. To date, the BCE has been demonstrated in various systems such as shape memory alloys [4–7], superionic compounds [8–10], and organic-inorganic hybrid perovskites [11–14]. In recent years, plastic crystals have received growing interest since the discovery of colossal BCEs in these materials [15–25]. These plastic crystals exhibit a unique structural duality: their molecular or ionic subunits display orientational disorder while maintaining long-range positional order in their center of mass. The orientational disorder-order phase transitions in plastic crystals combined with their high compressibility and strong anharmonicity enable giant isothermal entropy changes, positioning them ideal candidates for BCE-driven refrigeration [15].

However, most known caloric materials exhibit a relatively narrow operating temperature span [26]. For example, the prototype barocaloric material neopentylglycol exhibits only a modest increase of 10 K in the phase transition temperature from the cubic phase to the monoclinic phase when subjected to a pressure of 100 MPa [26]. This limitation—

where materials are functional only within a restricted temperature range—necessitates multi-stage configurations in caloric refrigerators to achieve broader cooling spans, leading to increased system complexity and costs [26]. Recently, this challenge has been overcome by the discovery of an all-temperature BCE in KPF_6 [26]. Remarkably, KPF_6 demonstrates an exceptionally wide BCE temperature span from 77 K to 300 K [26]. The all-temperature BCE is linked to persistent pressure-induced phase transitions, as corroborated by pressure-dependent neutron powder diffraction (NPD), Raman scattering analyses, and first-principles calculations [26].

While the temperature-pressure phase diagram for KPF_6 has been experimentally established through pressure-dependent Raman spectroscopy and neutron diffraction [26, 27], the atomistic mechanisms underlying the phase transitions across its four phases (see Fig. 1)—room-temperature face-centered cubic (C), intermediate-temperature monoclinic (M-II), low-temperature monoclinic (M-I), and high-pressure rhombohedral (R)—remain unresolved. Additionally, thorough investigations into the dynamic, thermodynamic, and electronic properties of these phases are lacking.

To address these gaps, we developed a robust machine-learning potential (MLP) for KPF_6 that can accurately describe all four phases across wide temperature and pressure ranges. This MLP enables accurate and efficient identification of crystal structures, exploration of dynamic and thermodynamic properties, and revelation of phase transitions under pressure. Phonon calculations confirm the dynamic stability of the M-II, M-I, and R phases at 0 K, with distinct flat phonon bands across broad frequency ranges arising mainly from PF_6 vibrations. In contrast, the thermally-disordered C phase displays pronounced anharmonicity and achieves dynamic stability only at elevated temperatures. Interestingly, the fluorine atoms within the PF_6 octahedra exhibit significant orientational disorder in the C phase. This disorder di-

* xingqiu.chen@imr.ac.cn

† ptliu@imr.ac.cn

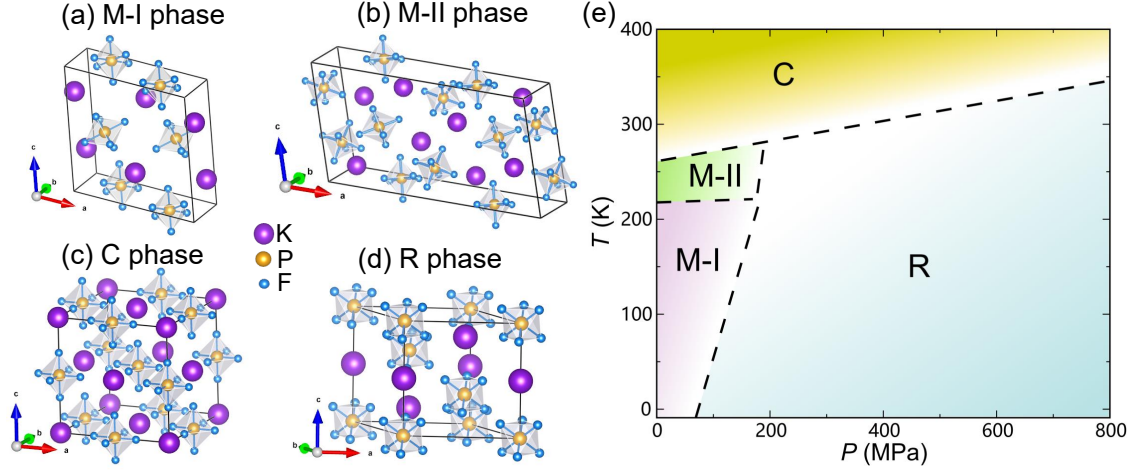


Figure 1. (a)-(d) Crystal structures of the four phases of KPF₆. (e) The experimentally-determined temperature-pressure phase diagram of KPF₆, adapted from Ref. [26].

minishes as the system transitions to the M-II phase at lower temperatures, and becomes suppressed in the M-I phase at 50 K. Under pressure, all the C, M-II, and M-I phases transform to the fully ordered R phase, leading to persistent isothermal entropy changes across a wide temperature range, which are responsible for the all-temperature BCE in this material. The phase transitions proceed through the cooperative rotation of the PF₆ octahedra accompanied by the lattice modulations. Finally, hybrid functional calculations of electronic band structures demonstrate wide-bandgap insulating behavior across all phases.

II. COMPUTATIONAL DETAILS

A. First-principles calculations

First-principles density functional theory (DFT) calculations were conducted using the Vienna *ab initio* simulation package (VASP) [28]. The interactions between nuclei and valence electrons were described by the projector augmented wave pseudopotentials recommended by VASP [29, 30]. We employed the PBEsol exchange-correlation functional [31], which typically provides an improved description of the equilibrium properties of solids [31]. To ensure convergence of the total energy to better than 1 meV/atom, a high plane wave energy cutoff of 700 eV was utilized. A Γ -centered k -point grid with a reciprocal-space resolution of 0.21 \AA^{-1} was used for sampling the Brillouin zone. The convergence criteria for total energy and ionic forces were set to 10^{-6} eV and 5 meV/ \AA , respectively. The Gaussian smearing method with a smearing width of 0.05 eV was applied. The electronic band structures were computed using the hybrid functional HSE06 [32]. Phonon dispersions and density of states were calculated using finite displacements with the Phonopy code [33]. To determine the energy barrier for phase transitions, we employed

the variable cell nudged elastic band (VCNEB) method [34].

B. Machine-learning potential development

The development of machine-learning potential followed the scheme outlined in our previous works [35–37]. Specifically, the training set generation consisted of two processes. The first process employed the on-the-fly active learning procedure as implemented in the VASP [38, 39]. This method is based on the kernel-based Bayesian regression and allows to automatically select the representative structures during the *ab initio* molecular dynamics (AIMD) simulations [38, 39]. The cutoff radii were set to 6 \AA and 5 \AA for the two-body and three-body descriptors, respectively. The number of radial basis functions was set to 10 for both the two-body and three-body descriptors. The width of the Gaussian functions used for broadening the atomic distributions of the descriptors was set to 0.5 \AA . The on-the-fly AIMD samplings were performed by heating the four phases of KPF₆ from 50 K to 600 K under pressures of 0, 0.5, and 1.0 GPa. The initial supercell structures were built with sixteen formula units based on the DFT relaxed structures. A time step of 2 fs was employed. The isothermal-isobaric ensemble was employed using a Langevin thermostat [40] combined with the Parrinello-Rahman method [41, 42].

The second process involved multiple active learning cycles utilizing the fitted moment tensor potential (MTP) [43], which is based on Shapeev’s generalized D-optimality criterion [44]. This approach leverages the high inference speed of the linearly parameterized MTP compared to kernel-based methods [45]. Additionally, the D-optimality criterion facilitates the efficient assessment of whether an unseen structure falls within the reliable interpolation regime or the risky extrapolation regime, eliminating the need for expensive DFT calculations *a priori* [44]. The active learning cycles started by generating initial structures that encompass a broad range of di-

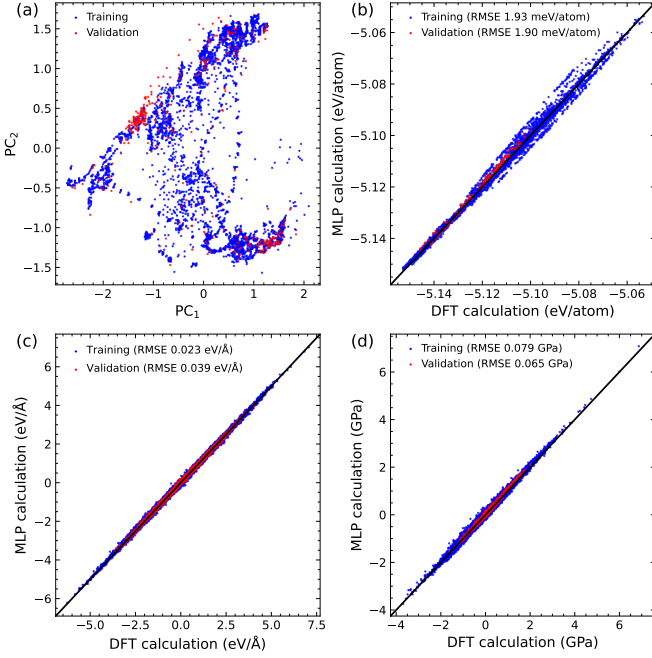


Figure 2. (a) The kernel principal component analysis of training and validation structures. (b)-(d) MLP predicted energies, forces, and stress tensors against DFT results. The training and validation datasets are indicated by the blue and red points, respectively.

versity, including the pristine four phases and the interpolated intermediate structures among them. Subsequently, a series of 200-ps MD simulations were performed at various temperatures and pressures using the LAMMPS code [46], interfaced with the MTP [47]. The Langevin thermostat [40] and the Parrinello-Rahman method [41, 42] were employed to control the temperature and pressure of the system, with a time step set to 2 fs. Configurations with an extrapolation grade exceeding 10 were identified, and the energies, forces, and stress tensors of these selected configurations were computed using PBEsol. These results were incorporated into the training set at the end of each active learning cycle, followed by a refitting of the MTP model. This iterative process continued until no configurations reached the specified threshold for extrapolation grade. To enhance efficiency, the MTP was fitted with optimized basis sets by refining the contraction process of moment tensors using our in-house code (IMR-MLP) [48]. This refinement significantly accelerates calculations without sacrificing accuracy [48]. When constructing the MTP basis functions, a cutoff radius of 6.0 Å was employed, with the number of radial basis functions set to 8. The maximum number of moment tensors involved in contraction was limited to 4, allowing for the consideration of up to five-body interactions. Through these multiple active learning cycles, the sampled phase space was significantly enhanced, resulting in improved transferability of the MTP.

The eventual training dataset includes 3418 structures. Additionally, a validation dataset consisting of 320 structures was constructed. These validation structures were randomly

sampled from MD simulations, as well as from structural perturbations applied to interpolated configurations between different phases. The training and validation structures were analyzed by principal component analysis (PCA) using the smooth overlap of atomic positions as local structure descriptors [49]. The kernel PCA analysis, as shown in Fig. 2(a), demonstrates that the validation dataset covers a fraction of the training set. The developed MTP exhibits a high accuracy, with validation root-mean-square errors for energies, forces, and stress tensors being 1.90 meV/atom, 0.039 eV/Å, and 0.065 GPa, respectively [see Figs. 2(b)-(d)].

C. Entropy calculations

Considering that the vibrational-orientational couplings are normally negligible, the total entropy S at pressure p and temperature T can be expressed as [24]

$$S(p, T) = S_{\text{vib}}(p, T) + S_{\text{ori}}(p, T), \quad (1)$$

where S_{vib} and S_{ori} represent the vibrational and orientational contributions, respectively.

The vibrational entropy S_{vib} is computed by [24]

$$S_{\text{vib}}(p, T) = -3N_{\text{at}}k_B \int_0^\infty \ln \left[2 \sinh \left(\frac{\hbar\omega}{2k_B T} \right) \right] \rho(\omega, p) d\omega + 3N_{\text{at}} \int_0^\infty \frac{\hbar\omega}{2T} \tanh^{-1} \left(\frac{\hbar\omega}{2k_B T} \right) \rho(\omega, p) d\omega. \quad (2)$$

Here, N_{at} is the number of atoms in the simulation cell, k_B is the Boltzmann's constant, \hbar is the reduced Planck constant, and $\rho(\omega, p)$ represents the vibrational density of states, which is estimated as the Fourier transform of the velocity autocorrelation function $C_v(t, p)$

$$\rho(\omega, p) = \int_0^\infty C_v(t, p) e^{i\omega t} dt. \quad (3)$$

The $C_v(t, p)$ was calculated using velocity data obtained from a 20 ps MD trajectory in the NpT ensemble, sampled at intervals of 5 fs.

The orientational entropy S_{ori} is calculated as follows. We first compute the quaternions $q = \{w, x, y, z\}$ representing the rotation of each PF₆ octahedron and restrict the domain to $w > 0$ since q and $-q$ represent the same rotation. Assuming each PF₆ octahedron rotates independently, the orientational entropy per PF₆ octahedron can be calculated as

$$S_{\text{ori}} = -k_B \int_{\mathbb{S}_+^3} P(q) \ln P(q) dq, \quad (4)$$

where $P(q)$ is the probability distribution function of the rotation quaternions, and the integration is performed over the positive hemisphere of the 3-sphere, denoted as \mathbb{S}_+^3 . In practical calculations, we constructed a uniform Fibonacci grid

Table I. The lattice parameters of the four phases of KPF_6 predicted by PBEsol at 0 K and MD simulations at 300 K. The experimental data are given for comparison. It is important to note the experimental conditions under which the data were obtained for each phase: the M-I phase data were collected at 3.5 K and 0 GPa [26], the M-II phase data at 250 K and 0 GPa [26], the C phase data at 300 K and 0 GPa [27], and the R phase data at 10 K and 0.4 GPa [26].

		a (Å)	b (Å)	c (Å)	β/γ (°)
M-I ($C2/c$)	Cal. (0 K, 0 GPa)	9.655	5.106	9.617	104.00
	Exp. (3.5 K, 0 GPa)[26]	9.417	4.909	9.459	103.40
M-II (Cc)	Cal. (0 K, 0 GPa)	18.121	5.306	9.626	102.07
	Exp. (250 K, 0 GPa)[26]	18.130	5.384	9.583	101.08
C ($Fm\bar{3}m$)	Cal. (0 K, 0 GPa)	8.543	8.543	8.543	90.00
	Cal. (300 K, 0 GPa, MD)	8.071	8.071	8.071	90.00
	Exp. (300 K, 0 GPa)[27]	7.786	7.786	7.786	90.00
R ($R\bar{3}$)	Cal. (0 K, 0 GPa)	7.317	7.317	7.094	120.00
	Cal. (0 K, 0.4 GPa)	7.226	7.226	7.052	120.00
	Exp. (10 K, 0.4 GPa)[26]	7.096	7.096	7.005	120.00

over \mathbb{S}_+^3 using the algorithm described in Ref. [50]. The discrete form of Eq. (4) can thus be derived as

$$S_{\text{ori}} = -k_B \sum_{i=1}^{N_{\text{bins}}} \frac{n_i}{N} \ln \frac{n_i}{N} + k_B \ln \left(\frac{\pi^2}{N_{\text{bins}}} \right), \quad (5)$$

where N represents the total number of quaternion samples, N_{bins} is the number of histogram bins, and n_i denotes the count of samples in bin i . In practice, 4000 grid points were used to sample the quaternion space. Orientational data were sampled from a 5 ns NpT -MD trajectory using the supercells consisting of 2306 atoms for the M-I, M-II, and R phases, and 2048 atoms for the C phase.

III. RESULTS AND DISCUSSION

A. Crystal structures

Figure 1 depicts the crystal structures for the M-I, M-II, and R phases of KPF_6 and the experimentally-determined temperature-pressure phase diagram. The M-I phase is a low-temperature phase exhibiting a monoclinic crystal structure with the space group $C2/c$. The M-II phase represents an intermediate-temperature phase that also exhibits a monoclinic crystal structure, albeit with reduced symmetry (space group Cc). The C phase is the room-temperature phase, which possesses a face-centered cubic rock-salt structure. Lastly, the R phase is a high-pressure phase featuring a rhombohedral crystal structure with the space group $R\bar{3}$. The simulated X-ray diffraction (XRD) patterns of the four phases are presented in Supplementary Information Fig. S1 [51].

We note that the crystal structures of the C and R phases, including their symmetry and atomic positions, have been previously determined through temperature-dependent single-crystal XRD and NPD [26, 27]. In contrast, the M-I and M-II phases, which are characterized by lower crystal symmetries

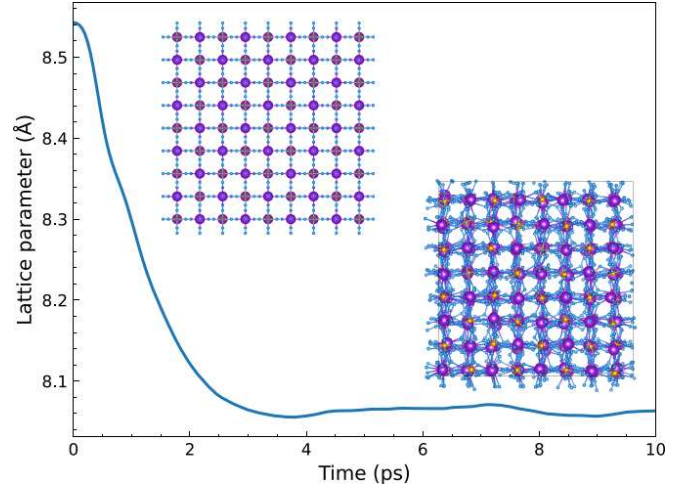


Figure 3. Time evolution of the lattice parameter for the C phase during a MD simulation at 300 K and 0 GPa. Insets show the top view of the initial configuration obtained from PBEsol relaxation and the final equilibrated configuration from the MD simulation, highlighting the plastic crystal nature of the C phase characterized by significant orientational disorder of the fluorine atoms.

and larger unit cells, pose significant challenges in identifying their space groups and atomic positions [27, 52]. This challenge has only been addressed recently [26] through the application of a MLP-accelerated generic structure search approach [53], combined with experimental constraint information [26]. Specifically, the experimental constraints, such as the minimum interatomic distances between different atom types, significantly reduced the search space, facilitating a more efficient and accurate determination of the complex crystal structures. The lattice parameters of the four phases of KPF_6 , predicted using the PBEsol functional, are provided in Table I. One can observe good agreement between the predicted values and the experimental results. For more detailed information regarding the crystal structures, we refer to the Supplementary Information Tables S1-S4 [51].

It is important to note that the highly symmetric structure of the C phase depicted in Fig. 1(c) is dynamically unstable at 0 K (Supplementary Information Fig. S2 [51]). In fact, this instability is indicative of fluorine orientational disorder (FOD), allowing it to be regarded as an ionic plastic crystal. The manifestation of diffuse scattering for this phase has been observed in neutron diffraction experiment [27]. Indeed, when conducting MD simulations at 300 K using the PBEsol-relaxed ordered structure as the initial configuration, the PF_6 octahedra exhibit strong FOD (see Fig. 3). This disorder leads to a reduction in lattice parameters, bringing them into closer alignment with the experimental values (see Table I).

B. Energetic properties

Figure 4(a) presents the energy-volume curves for the four phases of KPF_6 at 0 K predicted by PBEsol. As expected, the

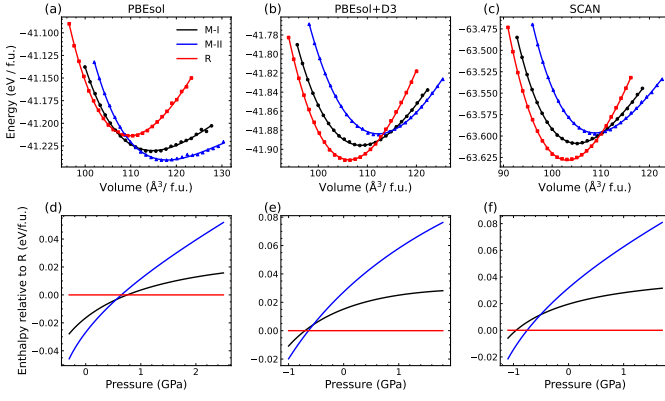


Figure 4. Energy-volume curves for the M-I, M-II, and R phases of KPF_6 , calculated at 0 K using the (a) PBEsol, (b) PBEsol+D3, and (c) SCAN functionals. (d)-(f) Corresponding enthalpy-pressure curves of the M-I and M-II phases relative to the R phase.

M-I and M-II phases have larger equilibrium volumes than the high-pressure R phase. The calculated transition pressures from M-II and M-I to the R phase are 0.66 GPa and 0.71 GPa, respectively [Fig. 4(d)]. We note that the C phase exhibits a significantly overestimated equilibrium volume and total energy at 0 K (Supplementary Information Fig. S3 [51]), which can be attributed to the neglect of vibrational and orientational disorder effects of the F atoms, as discussed earlier (Sec. III A). Notably, PBEsol incorrectly identifies the M-II phase as the ground state, contradicting experimental observations [26], though the energy difference between M-I and M-II is as small as 1.3 meV per atom.

Given the presence of FOD in KPF_6 , we also assessed the role of van der Waals (vdW) interactions. Including vdW corrections via Grimme’s D3 method [54] restores the correct energetic ordering between the M-I and M-II phases. However, PBEsol+D3 introduces a new discrepancy: it erroneously predicts the R phase as the ground state [Fig. 4(b)]. This means that a negative pressure is needed to induce the transition from the M-I and M-II phases to the R phase [Fig. 4(e)], again conflicting with experiments [26]. We further examined the strongly constrained appropriately normed (SCAN) functional [55], which yields energetics similar to PBEsol+D3 [Figs. 4(c) and (f)]. These results suggest that none of the tested exchange-correlation functionals can simultaneously describe all phases accurately. Since the pressure-driven phase transition is the primary focus of this work, we ultimately adopted the PBEsol functional, as it provides a more reliable description of the pressure-driven transition behavior despite its limitations in ground-state energetics.

C. Dynamical properties

The phonon dispersion relationships of the four phases of KPF_6 calculated using the MTP are shown in Fig. 5, exhibiting relatively flat and well-separated bands characteristic of plastic crystals with weak phonon-phonon interactions.

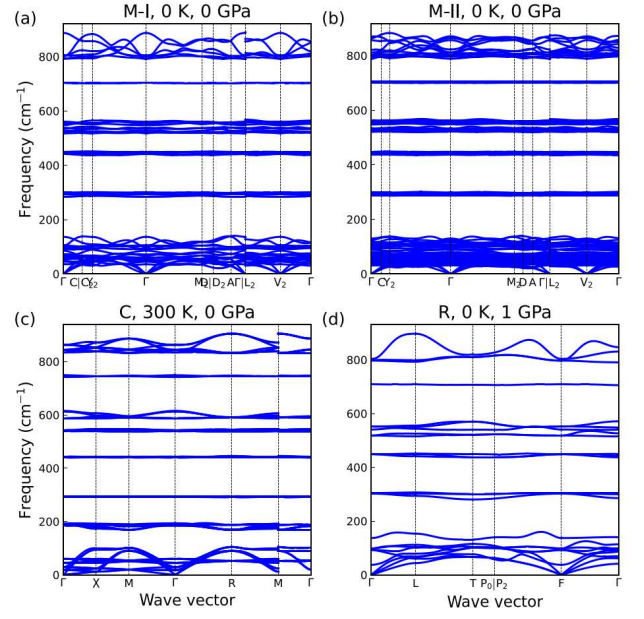


Figure 5. Phonon dispersion relationships of the four phases of KPF_6 calculated using the MTP. (a) The M-I phase at 0 K and 0 GPa. (b) The M-II phase at 0 K and 0 GPa. (c) The C phase at 300 K and 0 GPa (obtained by the SSCHA method). (d) The R phase at 0 K and 1 GPa.

The ground-state M-I phase is dynamically stable at 0 K and 0 GPa [Fig. 5(a)], as expected for the equilibrium structure. Interestingly, the intermediate-temperature M-II phase also maintains dynamical stability at 0 K [Fig. 5(b)], despite being the intermediate-temperature phase. In contrast, the high-temperature C phase is dynamically unstable at 0 K and 0 GPa, exhibiting imaginary phonon modes at the harmonic level (Supplementary Information Fig. S2 [51]), which reveals its strong anharmonicity. However, when anharmonic phonon-phonon interactions are included at 300 K using the stochastic self-consistent harmonic approximation (SSCHA) [56], the C phase becomes dynamically stable, consistent with experimental observations [26] [Fig. 5(c)]. Finally, the high-pressure R phase demonstrates dynamical stability at both 1 GPa [Fig. 5(d)] and 0 GPa (Supplementary Information Fig. S2 [51]), indicating its robust stability across pressure conditions.

We further analyzed the atomic contributions to the phonon modes. The computed atom-resolved phonon density of states (DOSs) for the four phases of KPF_6 are shown in Fig. 5. All four phases exhibit similar frequency ranges in their phonon DOSs. The K atoms primarily vibrate within the 200 cm^{-1} range, while the P atoms cover a relatively broad spectrum of frequencies, encompassing low, intermediate, and high frequencies. Notably, the F atoms dominate most frequency regions, with those flat phonon bands exclusively attributed to their vibrations. Since the four phases exhibit similar atom-resolved DOSs, we will focus only on the R phase as an example to detail the atomic contributions (Supplementary Information Fig. S4 [51]). The low-frequency phonon modes

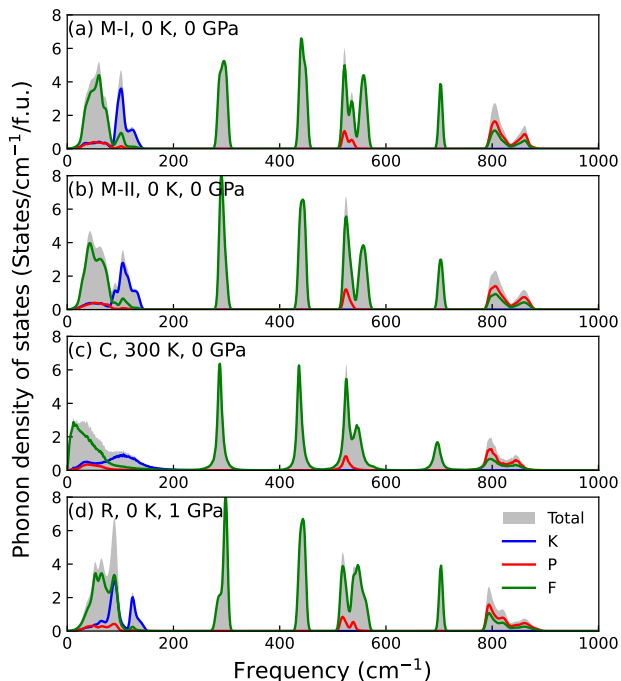


Figure 6. Atom-resolved phonon density of states of the four phases of KPF_6 calculated using the MTP. (a) The M-I phase at 0 K and 0 GPa. (b) The M-II phase at 0 K and 0 GPa. (c) The C phase at 300 K and 0 GPa (obtained by MD). (d) The R phase at 0 K and 1 GPa.

(below 200 cm^{-1}) arise from the rotation of the PF_6 octahedra and the vibration of K atoms. The phonon modes around 300 cm^{-1} and 470 cm^{-1} originate from the bending motions of the PF_6 octahedra, corresponding to the group representations of F_{2u} and F_{2g} , respectively. The phonon modes ranging from 500 to 600 cm^{-1} are associated with the asymmetric stretching and bending of the PF_6 octahedra. The separate strong peak at about 720 cm^{-1} is linked to the A_{1g} mode, which reflects the symmetric stretching vibration of the PF_6 octahedra. The highest phonon modes above 800 cm^{-1} correspond to the stretching of the PF_6 octahedra, accompanied by the vibrations of P atoms. These theoretical phonon mode analyses align well with the experimental Raman spectra results [26].

D. Pressure-induced phase transitions and entropy changes

Experimentally, all M-I, M-II, and C phases undergo phase transformations to the R phase upon pressure [26]. To estimate the energy barriers associated with these phase transitions, we calculated the enthalpy at 0 K and 1 GPa along the respective transformation pathways using the VCNEB method [34]. However, the VCNEB results are highly sensitive to the choice of the initial transformation pathway due to the facile rotation of the PF_6 octahedra, which can lead to slow convergence. To address this problem, we utilized a strain-minimum transformation pathway identified through the Crystmatch code [57] as our initial pathway. This ap-

proach resulted in minimal supercells containing 4, 8, and 4 formula units for the M-I, M-II, and C phases transitioning to the R phase, respectively. To further enhance convergence efficiency, we partitioned the initial reaction pathway into multiple segments and performed independent VCNEB optimizations for each segment. Convergence was deemed achieved when the maximum perpendicular forces fell below 0.02 eV/\AA .

The VCNEB results are displayed in Fig. 7. One can observe the non-smooth transformation pathways manifested by the emergence of numerous metastable phases, which is caused by the ease of PF_6 octahedral rotations coupled with lattice modulations. To better visualize the detailed phase transformation process, we direct the reader to the Supplementary Movies. Note that the exploration of such broad phase space during the energy barrier calculations has only been made possible by the developed accurate and efficient MTP. The maximum energy barriers for the M-I and M-II phases transitioning to the R phase are found to be comparable, with values of 0.09 eV/f.u. and 0.07 eV/f.u. , respectively. These values are low for typical solid-solid phase transitions, indicating that these pressure-induced transitions can occur with relative ease. Indeed, experimental studies have demonstrated that applying pressure in the range of just hundreds of MPa is sufficient to induce these phase transitions [26]. It is crucial to highlight that the VCNEB method is a zero-temperature method that does not account for the vibrational and orientational disorder effects. These effects are particularly significant for the high-temperature C phase as demonstrated in Fig. 3. Ignoring these effects would incorrectly result in a vanishing energy barrier for the transition from the C phase to the R phase [see Fig. 7(c)].

Despite the relatively low energy barriers in the pressure-induced phase transitions, the dynamic phase transformation process has proven challenging to reproduce through direct unbiased MD simulations over time scales of hundreds of picoseconds. This is largely due to the restricted time scales currently accessible in MD simulations, which may not adequately capture the dynamics of solid-solid phase transitions. Therefore, we will focus our discussion on the FOD and entropy of each phase at the specified temperature and pressure. To this end, we computed the angular probability density for the PF bonds (see Fig. 8) and temperature-dependent entropies for the four phases of KPF_6 at 0 GPa and 1 GPa (Fig. 9). Notably, the C phase at 300 K and 0 GPa exhibits the highest degree of FOD, characterized by predominant rotations of the PF_6 octahedra [Fig. 8(a)]. In the M-II phase at 300 K and 0 GPa, we observe a noticeable yet slightly decreasing level of FOD [Fig. 8(b)]. Interestingly, even in the M-I phase at 150 K and 0 GPa, some degree of FOD persists [Fig. 8(c)], which is only suppressed at the lower temperature of 50 K, where just local vibrations are present [Fig. 8(d)]. Applying a pressure of 1 GPa to the C, M-II, and M-I phases results in significant alterations to the fluorine orientation distributions, leading to a reduction in FOD. In particular, the FOD observed in the M-I phase at 150 K is completely suppressed under pressure [Fig. 8(g)]. In contrast, the high-pressure R phase exhibits a more ordered fluorine orientation, regardless of temperature

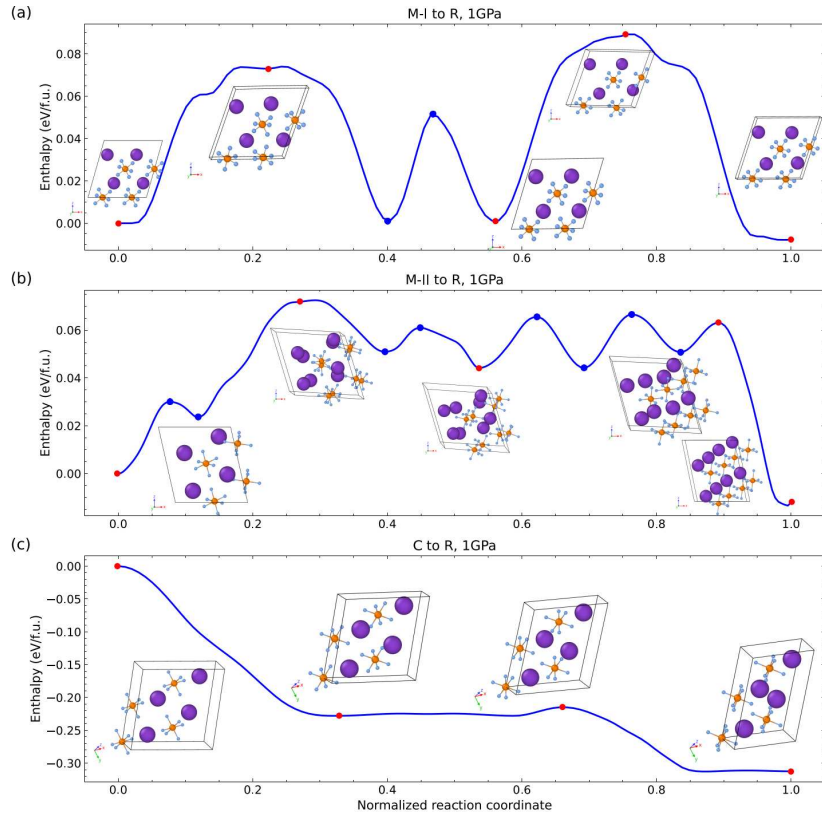


Figure 7. Energy barriers for the pressure-induced phase transitions from the M-I, M-II, and C phases to the R phase, calculated at 0 K and 1 GPa using the MTP with the VCNEB method. Insets display selected structures along the transformation pathways (corresponding to the images indicated by red points). The complete phase transformation processes are available for visualization in the Supplementary Movies.

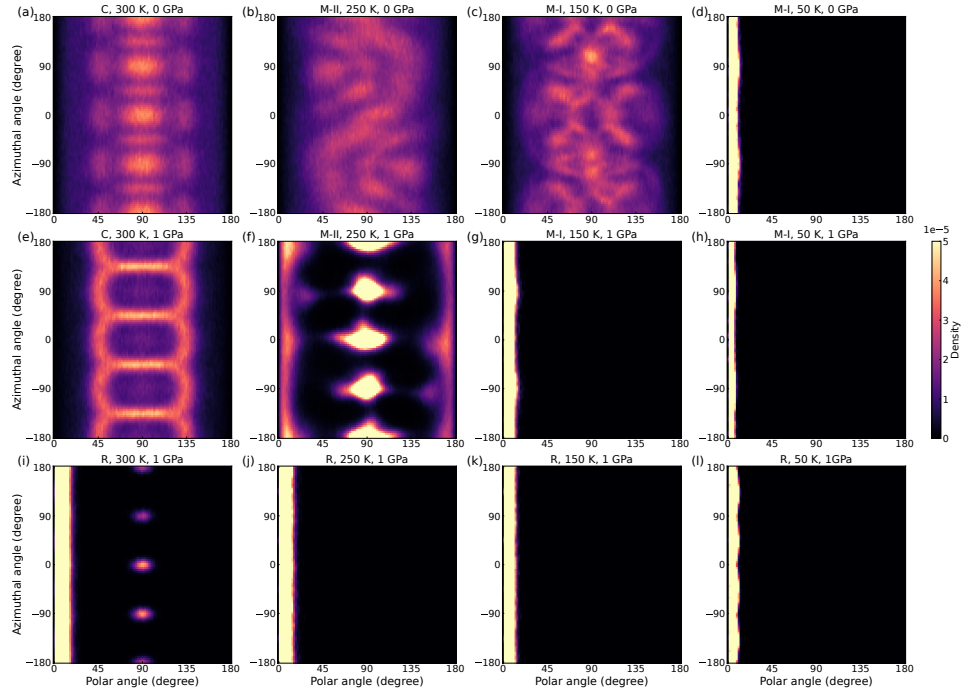


Figure 8. Angular probability density for the PF bonds in the four phases of KPF_6 at specific temperature and pressure, obtained from the MTP-accelerated MD simulations. The color coding highlights regions of high probability in light colors and low probability in dark colors.

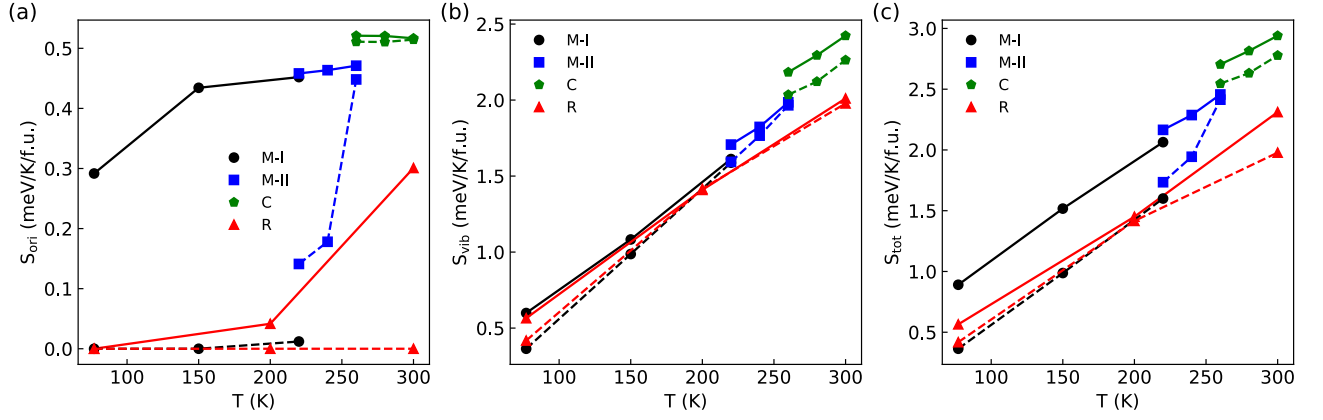


Figure 9. MTP-predicted temperature-dependent entropies for the four phases of KPF_6 at 0 GPa (solid lines) and 1 GPa (dashed lines). (a) Orientational entropy. (b) Vibrational entropy. (c) Total entropy.

variations [Figs. 8(i)-(l)], while weak PF_6 octahedra rotations are only observed at 300 K [Fig. 8(i)]. These results underscore the significant role of FOD in the phase transitions of KPF_6 .

The degree of FOD is quantitatively reflected by the predicted orientational entropy, as illustrated in Fig. 9(a). At 0 GPa, the orientational entropies decrease with the decreasing temperature, accompanied with the temperature-driven phase transitions from the C phase to the M-II phase to the M-I phase. When a pressure of 1 GPa is applied, there is an overall reduction in orientational entropies. This pressure effect is particularly pronounced in the M-I and R phases, where the FOD is nearly completely suppressed. In comparison to the orientational entropy, vibrational entropy is considerably larger and thus dominates the total entropy, as shown in Fig. 9(b). As expected, the vibrational entropy increases with temperature and decreases under pressure. The total entropies including both orientational and vibrational contributions are displayed in Fig. 9(c). Notably, within the considered temperature range of 77 to 300 K, there are persistent isothermal entropy changes upon pressure, which are associated with pressure-induced phase transitions from the C, M-II, and M-I phases to the fully ordered R phase. The isothermal entropy change is largest when transforming the C phase to the R phase under pressure, attributed to the plastic crystal nature of the C phase, which results in nearly equal contributions from both orientational and vibrational entropy changes. These findings align well with the experimental results, providing a comprehensive explanation for the observed all-temperature BCE in this material [26].

E. Electronic properties

Finally, we investigated the electronic properties of KPF_6 . Fig. 10 presents the electronic band structures of the four phases of KPF_6 calculated using the HSE06 functional. It is evident that all four phases exhibit a wide band gap of approximately 8 eV, indicating insulating behavior. Such a large

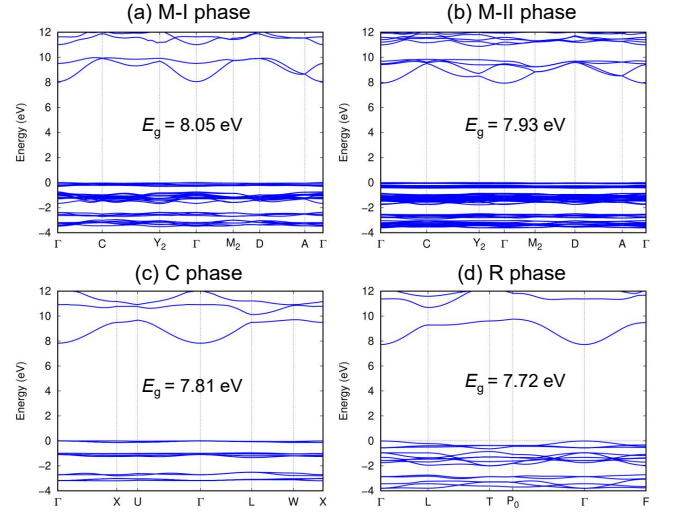


Figure 10. Electronic band structures of the four phases of KPF_6 calculated using the HSE06 functional. (a) The M-I phase. (b) The M-II phase. (c) The C phase. (d) The R phase. The structures are obtained at 0 K and 0 GPa using the PBEsol functional.

band gap results in low electrical conductivity, which is advantageous for practical applications of the BCE where efficient thermal management is crucial. The valence bands are featured by the flat bands, while the conduction bands are more dispersive. Atom-resolved electronic density of states analysis reveals that the bands near the gap are predominantly contributed by the fluorine atoms (Supplementary Information Fig. S5 [51]), highlighting their significant role also in the electronic properties of KPF_6 .

IV. CONCLUSION

In conclusion, this study has provided a comprehensive understanding of the atomistic mechanisms driving the phase transitions of KPF_6 through a combination of first-principles calculations and MLP-accelerated molecular dynamics simulations. We have identified four distinct phases of KPF_6 , each characterized by its dynamic stability, phonon modes, and varying degrees of FOD. Our findings indicate that the room-temperature C phase exhibits substantial FOD, while the intermediate-temperature M-II and low-temperature M-I phases demonstrate a progressive reduction in FOD as the temperature decreases. Notably, the application of pressure significantly suppresses the degree of FOD, leading to the emergence of the fully ordered R phase. Our analysis highlights the critical role of thermal fluctuations in stabilizing the C phase, whereas the M-II, M-I, and R phases exhibit inherent stability at 0 K. The interplay between FOD, anharmonic lattice dynamics, and cooperative octahedral rotations under pressure enables KPF_6 to achieve persistent isothermal entropy changes across a broad temperature range through pressure-induced phase transitions. These insights not only deepen our understanding of KPF_6 , but also pave the way for the design of advanced barocaloric materials with wide operating temperature spans.

DECLARATION OF COMPETING INTEREST

The authors declare that they have no known competing financial interests or personal relationships that could have ap-

peared to influence the work reported in this paper.

AUTHOR CONTRIBUTIONS

P.L. conceived the project. P.L. designed the research with the help of B.L. and X.-Q.C. J.W. and P. L. performed the calculations. P.L., B.L., and X.-Q.C. supervised the project. Y.-C.Z., Y.L., H.D., M.L., and Y.S. participated in discussions. P.L. wrote the manuscript with inputs from other authors. All authors comments on the manuscript.

ACKNOWLEDGEMENTS

This work is supported by the National Natural Science Foundation of China (Grants No. 52422112, No. 52188101, and No. 52201030), the Strategic Priority Research Program of the Chinese Academy of Sciences (XDA041040402), the Liaoning Province Science and Technology Major Project (2024JH1/11700032, 2023021207-JH26/103 and RC230958), the National Key R&D Program of China 2021YFB3501503, and the Special Projects of the Central Government in Guidance of Local Science and Technology Development (2024010859-JH6/1006).

-
- [1] B. G. Shen, J. R. Sun, F. X. Hu, H. W. Zhang, and Z. H. Cheng, "Recent progress in exploring magnetocaloric materials," *Advanced Materials* **21**, 4545–4564 (2009).
 - [2] J.F. Scott, "Electrocaloric materials," *Annual Review of Materials Research* **41**, 229–240 (2011).
 - [3] Lluís Mañosa and Antoni Planes, "Materials with giant mechanocaloric effects: Cooling by strength," *Advanced Materials* **29**, 1603607 (2017).
 - [4] Lluís Mañosa, David González-Alonso, Antoni Planes, Er-ell Bonnot, Maria Barrio, Josep-Lluís Tamarit, Seda Aksoy, and Mehmet Acet, "Giant solid-state barocaloric effect in the Ni–Mn–In magnetic shape-memory alloy," *Nature Materials* **9**, 478–481 (2010).
 - [5] Luca Cirillo, Adriana Greco, and Claudia Masselli, "Cooling through barocaloric effect: A review of the state of the art up to 2022," *Thermal Science and Engineering Progress* **33**, 101380 (2022).
 - [6] Araceli Aznar, Adrià Gràcia-Condal, Antoni Planes, Pol Lloveras, Maria Barrio, Josep-Lluís Tamarit, Wenxin Xiong, Daoyong Cong, Catalin Popescu, and Lluís Mañosa, "Giant barocaloric effect in all-*d*-metal heusler shape memory alloys," *Physical Review Materials* **3**, 044406 (2019).
 - [7] Enric Stern-Taulats, Antoni Planes, Pol Lloveras, Maria Barrio, Josep-Lluís Tamarit, Sabyasachi Pramanick, Subham Majumdar, Suheyla Yüce, Baris Emre, Carlos Frontera, and Lluís Mañosa, "Tailoring barocaloric and magnetocaloric properties in low-hysteresis magnetic shape memory alloys," *Acta Materialia* **96**, 324–332 (2015).
 - [8] Claudio Cazorla and Daniel Errandonea, "Giant mechanocaloric effects in fluorite-structured superionic materials," *Nano Letters* **16**, 3124–3129 (2016).
 - [9] Araceli Aznar, Pol Lloveras, Michela Romanini, María Barrio, Josep-Lluís Tamarit, Claudio Cazorla, Daniel Errandonea, Neil D. Mathur, Antoni Planes, Xavier Moya, and Lluís Mañosa, "Giant barocaloric effects over a wide temperature range in superionic conductor AgI ," *Nature Communications* **8**, 1851 (2017).
 - [10] Jie Min, Arun K. Sagotra, and Claudio Cazorla, "Large barocaloric effects in thermoelectric superionic materials," *Phys. Rev. Mater.* **4**, 015403 (2020).
 - [11] Juan M. Bermúdez-García, Manuel Sánchez-Andújar, Socorro Castro-García, Jorge López-Beceiro, Ramón Artiaga, and María A. Señarís-Rodríguez, "Giant barocaloric effect in the ferroic organic-inorganic hybrid $[\text{TPrA}][\text{Mn}(\text{dca})_3]$ perovskite under easily accessible pressures," *Nature Communications* **8**, 15715 (2017).
 - [12] Juan M. Bermúdez-García, Manuel Sánchez-Andújar, and María A. Señarís-Rodríguez, "A new playground for organic–inorganic hybrids: Barocaloric materials for pressure-induced solid-state cooling," *The Journal of Physical Chemistry Letters*

- 8, 4419–4423 (2017).
- [13] Jorge Salgado-Beceiro, Ariel Nonato, Rosivaldo Xavier Silva, Alberto García-Fernández, Manuel Sánchez-Andújar, Socorro Castro-García, Enric Stern-Taulats, María Antonia Señaris-Rodríguez, Xavier Moya, and Juan Manuel Bermúdez-García, “Near-room-temperature reversible giant barocaloric effects in $[(\text{CH}_3)_4\text{N}]\text{Mn}[\text{N}_3]_3$ hybrid perovskite,” *Materials Advances* **1**, 3167–3170 (2020).
 - [14] Junning Li, María Barrio, David J. Dunstan, Richard Dixey, Xiaojie Lou, Josep-Lluís Tamarit, Anthony E. Phillips, and Pol Lloveras, “Colossal reversible barocaloric effects in layered hybrid perovskite $(\text{C}_{10}\text{H}_{21}\text{NH}_3)_2\text{MnCl}_4$ under low pressure near room temperature,” *Advanced Functional Materials* **31**, 2105154 (2021).
 - [15] Bing Li, Yukinobu Kawakita, Seiko Ohira-Kawamura, Takeshi Sugahara, Hui Wang, Jingfan Wang, Yanna Chen, Saori I. Kawaguchi, Shogo Kawaguchi, Koji Ohara, Kuo Li, Dehong Yu, Richard Mole, Takanori Hattori, Tatsuya Kikuchi, Shin-ichiro Yano, Zhao Zhang, Zhe Zhang, Weijun Ren, Shangchao Lin, Osami Sakata, Kenji Nakajima, and Zhidong Zhang, “Colossal barocaloric effects in plastic crystals,” *Nature* **567**, 506–510 (2019).
 - [16] P. Lloveras, A. Aznar, M. Barrio, Ph. Negrier, C. Popescu, A. Planes, L. Mañosa, E. Stern-Taulats, A. Avramenko, N. D. Mathur, X. Moya, and J.-Ll. Tamarit, “Colossal barocaloric effects near room temperature in plastic crystals of neopentylglycol,” *Nature Communications* **10**, 1803 (2019).
 - [17] Araceli Aznar, Pol Lloveras, María Barrio, Philippe Negrier, Antoni Planes, Lluís Mañosa, Neil D. Mathur, Xavier Moya, and Josep-Lluís Tamarit, “Reversible and irreversible colossal barocaloric effects in plastic crystals,” *Journal of Materials Chemistry A* **8**, 639–647 (2020).
 - [18] F. B. Li, M. Li, X. Xu, Z. C. Yang, H. Xu, C. K. Jia, K. Li, J. He, B. Li, and Hui Wang, “Understanding colossal barocaloric effects in plastic crystals,” *Nature Communications* **11**, 4190 (2020).
 - [19] Kartik Sau, Tamio Ikeshoji, Shigeyuki Takagi, Shin-ichi Orimo, Daniel Errandonea, Dewei Chu, and Claudio Cazorla, “Colossal barocaloric effects in the complex hydride $\text{Li}_2\text{B}_{12}\text{H}_{12}$,” *Scientific Reports* **11**, 11915 (2021).
 - [20] Qingyong Ren, Ji Qi, Dehong Yu, Zhe Zhang, Ruiqi Song, Wenli Song, Bao Yuan, Tianhao Wang, Weijun Ren, Zhidong Zhang, Xin Tong, and Bing Li, “Ultrasensitive barocaloric material for room-temperature solid-state refrigeration,” *Nature Communications* **13**, 2293 (2022).
 - [21] Alejandro Salvatori, Philippe Negrier, Araceli Aznar, María Barrio, Josep Lluís Tamarit, and Pol Lloveras, “Colossal barocaloric effects in adamantane derivatives for thermal management,” *APL Materials* **10**, 111117 (2022).
 - [22] Kun Zhang, Ruiqi Song, Ji Qi, Zhe Zhang, Zhao Zhang, Chenyang Yu, Kuo Li, Zhidong Zhang, and Bing Li, “Colossal barocaloric effect in carboranes as a performance tradeoff,” *Advanced Functional Materials* **32**, 2112622 (2022).
 - [23] Zhe Zhang, Kuo Li, Shangchao Lin, Ruiqi Song, Dehong Yu, Yida Wang, Jingfan Wang, Shogo Kawaguchi, Zhao Zhang, Chenyang Yu, Xiaodong Li, Jie Chen, Lunhua He, Richard Mole, Bao Yuan, Qingyong Ren, Kun Qian, Zhuangli Cai, Jingui Yu, Mingchao Wang, Changying Zhao, Xin Tong, Zhidong Zhang, and Bing Li, “Thermal batteries based on inverse barocaloric effects,” *Science Advances* **9**, eadd0374 (2023).
 - [24] Carlos Escorihuela-Sayalero, Luis Carlos Pardo, Michela Romanini, Nicolas Obrecht, Sophie Loehlé, Pol Lloveras, Josep-Lluís Tamarit, and Claudio Cazorla, “Prediction and understanding of barocaloric effects in orientationally disordered materials from molecular dynamics simulations,” *npj Computational Materials* **10**, 13 (2024).
 - [25] Samantha L. Piper, Leena Melag, Mega Kar, Azra Sourjah, Xiong Xiao, Eric F. May, Kondo-Francois Aguey-Zinsou, Douglas R. MacFarlane, and Jennifer M. Pringle, “Organic ionic plastic crystals having colossal barocaloric effects for sustainable refrigeration,” *Science* **387**, 56–62 (2025).
 - [26] Xueting Zhao, Zhao Zhang, Takanori Hattori, Jiantao Wang, Lingli Li, Yating Jia, Wanwu Li, Jianing Xue, Xiaoyan Fan, Ruiqi Song, Jinlong Zhu, Peitao Liu, Xing-Qiu Chen, Zhidong Zhang, and Bing Li, “All-temperature barocaloric effects at pressure-induced phase transitions,” *Nature Communications* **16**, 7713 (2025).
 - [27] Zhao Zhang, Xiaoming Jiang, Takanori Hattori, Xiong Xu, Min Li, Chenyang Yu, Zhe Zhang, Dehong Yu, Richard Mole, Shin-ichiro Yano, Jie Chen, Lunhua He, Chin-Wei Wang, Hui Wang, Bing Li, and Zhidong Zhang, “A colossal barocaloric effect induced by the creation of a high-pressure phase,” *Materials Horizons* **10**, 977–982 (2023).
 - [28] G. Kresse and J. Furthmüller, “Efficient iterative schemes for ab initio total-energy calculations using a plane-wave basis set,” *Phys. Rev. B* **54**, 11169–11186 (1996).
 - [29] P. E. Blöchl, “Projector augmented-wave method,” *Phys. Rev. B* **50**, 17953–17979 (1994).
 - [30] G. Kresse and D. Joubert, “From ultrasoft pseudopotentials to the projector augmented-wave method,” *Phys. Rev. B* **59**, 1758–1775 (1999).
 - [31] John P. Perdew, Adrienn Ruzsinszky, Gábor I. Csonka, Oleg A. Vydrov, Gustavo E. Scuseria, Lucian A. Constantin, Xiaolan Zhou, and Kieron Burke, “Restoring the density-gradient expansion for exchange in solids and surfaces,” *Phys. Rev. Lett.* **100**, 136406 (2008).
 - [32] Aliaksandr V. Krakau, Oleg A. Vydrov, Artur F. Izmaylov, and Gustavo E. Scuseria, “Influence of the exchange screening parameter on the performance of screened hybrid functionals,” *The Journal of Chemical Physics* **125**, 224106 (2006).
 - [33] Atsushi Togo and Isao Tanaka, “First principles phonon calculations in materials science,” *Scripta Materialia* **108**, 1–5 (2015).
 - [34] Guang-Rui Qian, Xiao Dong, Xiang-Feng Zhou, Yongjun Tian, Artem R. Oganov, and Hui-Tian Wang, “Variable cell nudged elastic band method for studying solid–solid structural phase transitions,” *Computer Physics Communications* **184**, 2111–2118 (2013).
 - [35] Peitao Liu, Jiantao Wang, Noah Avargues, Carla Verdi, Andreas Singraber, Ferenc Karsai, Xing-Qiu Chen, and Georg Kresse, “Combining machine learning and many-body calculations: coverage-dependent adsorption of CO on Rh(111),” *Physical Review Letters* **130**, 078001 (2023).
 - [36] Mingfeng Liu, Jiantao Wang, Junwei Hu, Peitao Liu, Haiyang Niu, Xuexi Yan, Jiangxu Li, Haile Yan, Bo Yang, Yan Sun, Chunlin Chen, Georg Kresse, Liang Zuo, and Xing-Qiu Chen, “Layer-by-layer phase transformation in Ti_3O_5 revealed by machine-learning molecular dynamics simulations,” *Nature Communications* **15**, 3079 (2024).
 - [37] Yu Cao, Jiantao Wang, Mingfeng Liu, Yan Liu, Hui Ma, Cesare Franchini, Yan Sun, Georg Kresse, Xing-Qiu Chen, and Peitao Liu, “Quantum delocalization enables water dissociation on Ru(0001),” *Phys. Rev. Lett.* **134**, 178001 (2025).
 - [38] Ryosuke Jinnouchi, Jonathan Lahnsteiner, Ferenc Karsai, Georg Kresse, and Menno Bokdam, “Phase transitions of hybrid perovskites simulated by machine-learning force fields trained on the fly with bayesian inference,” *Physical Review Letters* **122**, 225701 (2019).

- [39] Ryosuke Jinnouchi, Ferenc Karsai, and Georg Kresse, “On-the-fly machine learning force field generation: application to melting points,” *Physical Review B* **100**, 014105 (2019).
- [40] Michael P. Allen and Friederike Schmid, “A thermostat for molecular dynamics of complex fluids,” *Molecular Simulation* **33**, 21–26 (2007).
- [41] M. Parrinello and A. Rahman, “Crystal structure and pair potentials: A molecular-dynamics study,” *Physical Review Letters* **45**, 1196–1199 (1980).
- [42] M. Parrinello and A. Rahman, “Polymorphic transitions in single crystals: A new molecular dynamics method,” *Journal of Applied Physics* **52**, 7182–7190 (1981).
- [43] Alexander V. Shapeev, “Moment tensor potentials: a class of systematically improvable interatomic potentials,” *Multiscale Modeling & Simulation* **14**, 1153–1173 (2016).
- [44] Evgeny V. Podryabinkin and Alexander V. Shapeev, “Active learning of linearly parametrized interatomic potentials,” *Computational Materials Science* **140**, 171–180 (2017).
- [45] Yunxing Zuo, Chi Chen, Xiangguo Li, Zhi Deng, Yiming Chen, Jörg Behler, Gábor Csányi, Alexander V. Shapeev, Aidan P. Thompson, Mitchell A. Wood, and Shyue Ping Ong, “A performance and cost assessment of machine learning interatomic potentials,” *The Journal of Physical Chemistry A* **124**, 731–745 (2020).
- [46] Aidan P. Thompson, H. Metin Aktulga, Richard Berger, Dan S. Bolintineanu, W. Michael Brown, Paul S. Crozier, Pieter J. In ’t Veld, Axel Kohlmeyer, Stan G. Moore, Trung Dac Nguyen, Ray Shan, Mark J. Stevens, Julien Tranchida, Christian Trott, and Steven J. Plimpton, “LAMMPS - a flexible simulation tool for particle-based materials modeling at the atomic, meso, and continuum scales,” *Computer Physics Communications* **271**, 108171 (2022).
- [47] Ivan S Novikov, Konstantin Gubaev, Evgeny V Podryabinkin, and Alexander V Shapeev, “The MLIP package: moment tensor potentials with MPI and active learning,” *Machine Learning: Science and Technology* **2**, 025002 (2021).
- [48] Jiantao Wang, Peitao Liu, Heyu Zhu, Mingfeng Liu, Hui Ma, Yun Chen, Yan Sun, and Xing-Qiu Chen, “Efficient moment tensor machine-learning interatomic potential for accurate description of defects in Ni-Al alloys,” *Phys. Rev. Mater.* **9**, 053805 (2025).
- [49] Bingqing Cheng, Ryan-Rhys Griffiths, Simon Wengert, Christian Kunkel, Tamas Stenczel, Bonan Zhu, Volker L. Deringer, Noam Bernstein, Johannes T. Margraf, Karsten Reuter, and Gabor Csanyi, “Mapping materials and molecules,” *Accounts of Chemical Research* **53**, 1981–1991 (2020).
- [50] Marc Alexa, “Super-fibonacci spirals: Fast, low-discrepancy sampling of $so(3)$,” in *2022 IEEE/CVF Conference on Computer Vision and Pattern Recognition (CVPR)* (2022) pp. 8281–8290.
- [51] See Supplemental Material for the details of crystallographic information of the four phases of KPF_6 , simulated X-ray diffraction patterns, additional phonon dispersion relationships of the C and R phases at 0 K and 0 GPa, additional energy-volume curves including the C phase, phonon mode analysis of the R phase, and element-resolved electronic density of states.
- [52] P. Huber, Krummeck, Baller, Krüger, Knorr, , and S. Haussühl, “Phases and phase transitions of KPF_6 ,” *Ferroelectrics* **203**, 211–219 (1997).
- [53] Colin W. Glass, Artem R. Oganov, and Nikolaus Hansen, “USPEX—Evolutionary crystal structure prediction,” *Computer Physics Communications* **175**, 713–720 (2006).
- [54] Stefan Grimme, Jens Antony, Stephan Ehrlich, and Helge Krieg, “A consistent and accurate ab initio parametrization of density functional dispersion correction (DFT-D) for the 94 elements H-Pu,” *The Journal of Chemical Physics* **132**, 154104 (2010).
- [55] Jianwei Sun, Adrienn Ruzsinszky, and John P. Perdew, “Strongly constrained and appropriately normed semilocal density functional,” *Phys. Rev. Lett.* **115**, 036402 (2015).
- [56] Lorenzo Monacelli, Raffaello Bianco, Marco Cherubini, Matteo Calandra, Ion Errea, and Francesco Mauri, “The stochastic self-consistent harmonic approximation: Calculating vibrational properties of materials with full quantum and anharmonic effects,” *J. Phys.: Condens. Matter* **33**, 363001 (2021).
- [57] Fang-Cheng Wang, Qi-Jun Ye, Yu-Cheng Zhu, and Xin-Zheng Li, “Crystal-structure matches in solid-solid phase transitions,” *Phys. Rev. Lett.* **132**, 086101 (2024).

Supplemental Material to
“Atomistic mechanisms of phase transitions in all-temperature barocaloric material KPF_6 ”

Jiantao Wang,^{1,2} Yi-Chi Zhang,^{1,2} Yan Liu,^{1,2} Hongkun Deng,^{1,2}
Mingfeng Liu,¹ Yan Sun,¹ Bing Li,¹ Xing-Qiu Chen,^{1,*} and Peitao Liu^{1,†}

¹*Shenyang National Laboratory for Materials Science, Institute of Metal Research,
Chinese Academy of Sciences, 110016 Shenyang, China*

²*School of Materials Science and Engineering, University of Science and Technology of China, 110016 Shenyang, China*

* xingqiu.chen@imr.ac.cn

† ptliu@imr.ac.cn

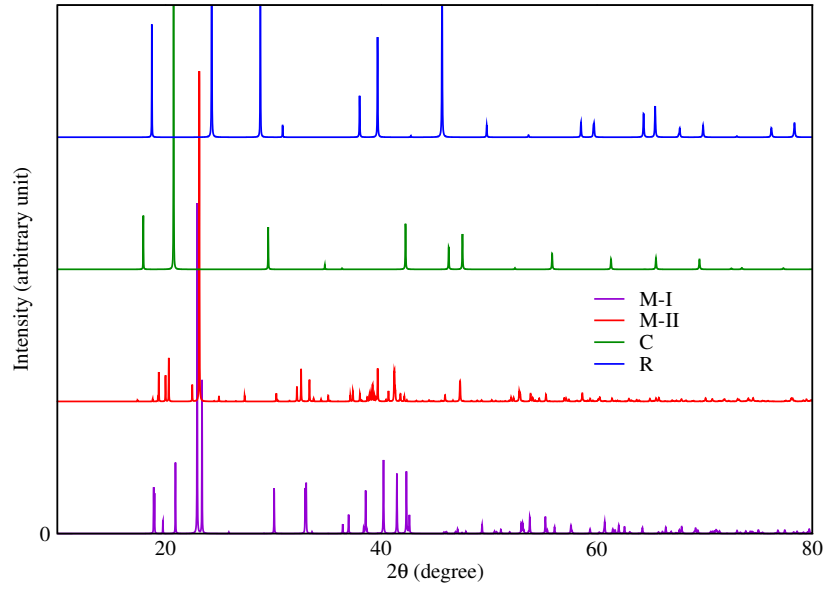


Figure S1. Simulated X-ray diffraction patterns of the four phases of KPF_6 using the $\text{Cu } K_\alpha$ radiation. The structures are obtained at 0 K and 0 GPa using the PBEsol functional.

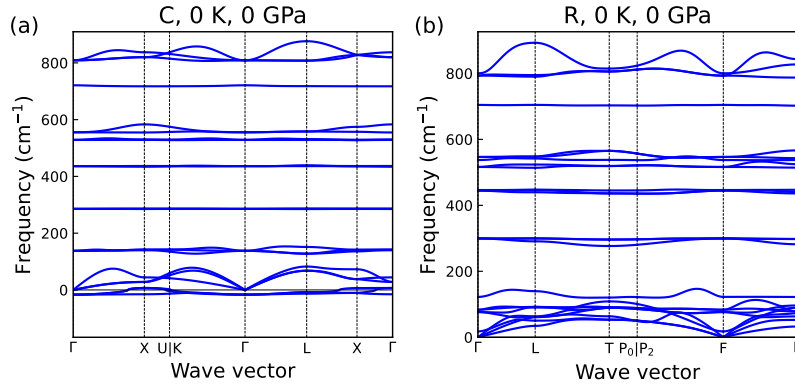


Figure S2. Phonon dispersion relationships of (a) the C phase and (b) the R phase at 0 K and 0 GPa predicted using the PBEsol-derived MTP.

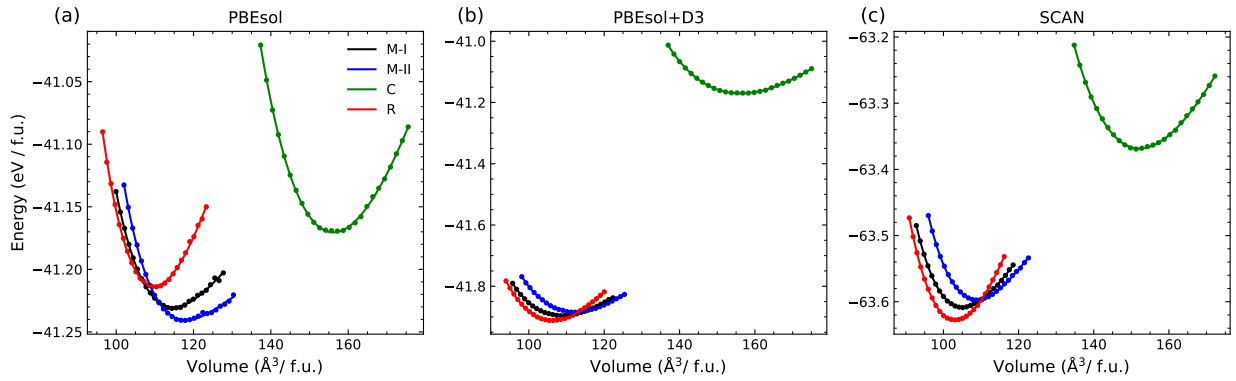


Figure S3. Energy-volume curves for the four phases of KPF_6 , calculated at 0 K using the (a) PBEsol, (b) PBEsol+D3, and (c) SCAN functionals.

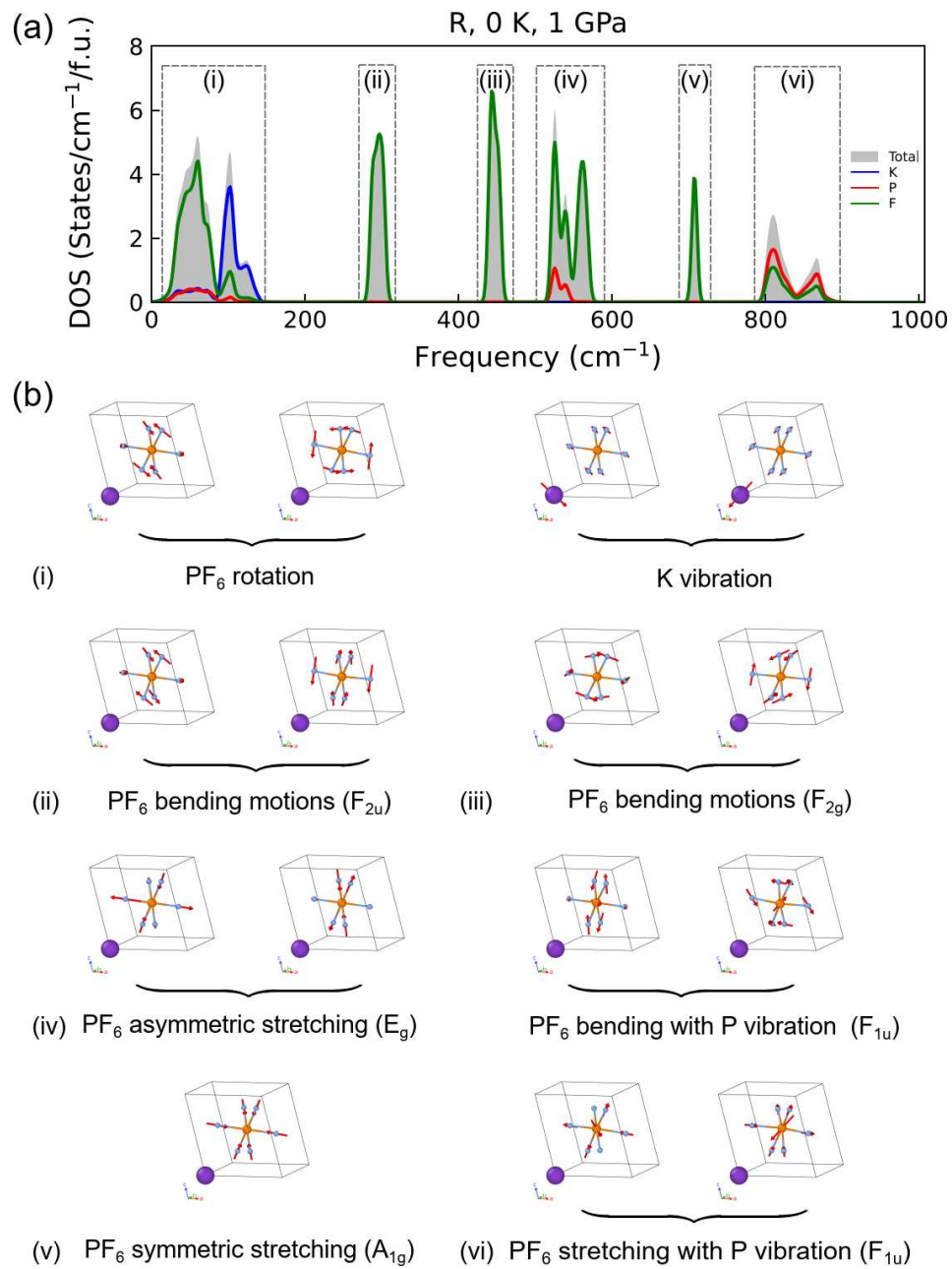


Figure S4. The phonon mode analysis of the R phase of KPF_6 , which is similar to those of the M -I, M -II, and C phases.

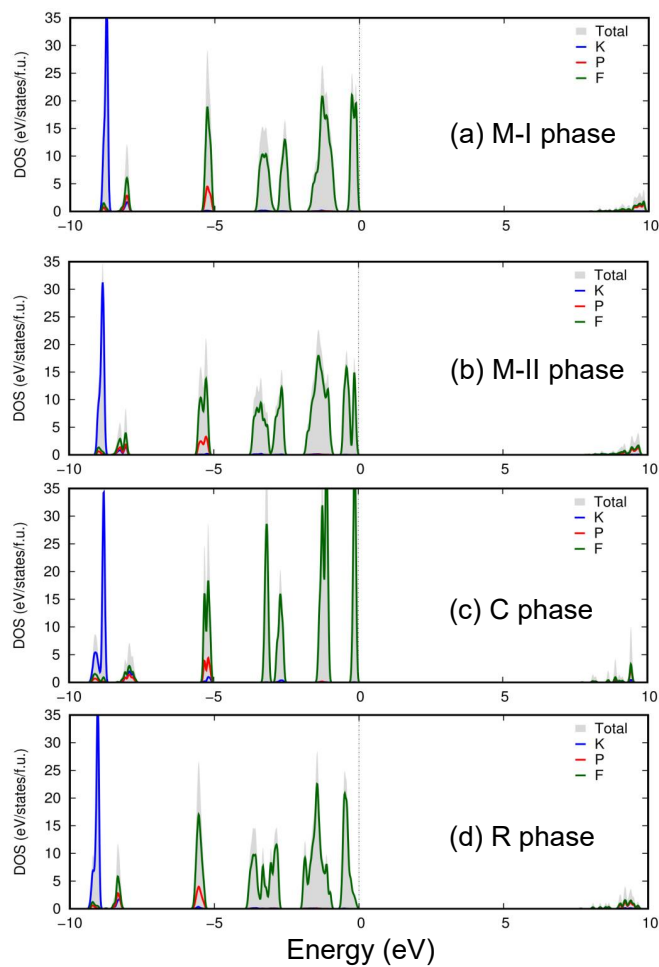


Figure S5. Electronic density of states of the four phases of KPF_6 calculated using the HSE06 functional. The structures are obtained at 0 K and 0 GPa using the PBEsol functional.

Table S1. Crystallographic information of the M-I phase of KPF_6 predicted by PBEsol at 0 K and 0 GPa.

Space group	a (Å)	b (Å)	c (Å)	β (°)
$C2/c$	9.655	5.106	9.617	104.00
Atomic positions				
Atoms	Site	x	y	z
K	4e	0.00000	0.33266	0.25000
P	4c	0.25000	0.25000	0.00000
F	8f	0.15534	0.49628	0.03271
F	8f	0.89330	0.12212	0.60295
F	8f	0.28025	0.40577	0.86241

Table S2. Crystallographic information of the M-II phase of KPF_6 predicted by PBEsol at 0 K and 0 GPa.

Space group	a (Å)	b (Å)	c (Å)	β (°)
Cc	18.121	5.306	9.626	102.07
Atomic positions				
Atoms	Site	x	y	z
K	4a	0.12182	0.18750	0.15100
K	4a	0.38284	0.32796	0.86604
P	4a	0.75033	0.25663	0.00616
P	4a	-0.00103	0.32409	0.74145
F	4a	0.75331	0.14984	0.84841
F	4a	0.74752	0.36175	0.16394
F	4a	0.32880	0.39216	0.57190
F	4a	0.17176	0.09503	0.44031
F	4a	0.79802	0.49729	0.47802
F	4a	0.20225	0.48968	0.53343
F	4a	0.41395	0.16611	0.27250
F	4a	0.08444	0.31157	0.71173
F	4a	0.52657	0.33539	0.38779
F	4a	-0.02104	0.05918	0.65500
F	4a	0.47091	0.02132	0.09464
F	4a	0.51969	0.08771	0.82658

Table S3. Crystallographic information of the C phase of KPF_6 predicted by PBEsol at 0 K and 0 GPa.

Space group	a (Å)	b (Å)	c (Å)	β (°)
$Fm\bar{3}m$	8.543	8.543	8.543	90.00
Atomic positions				
Atoms	Site	x	y	z
K	4a	0.00000	0.00000	0.00000
P	4b	0.50000	0.50000	0.50000
F	24c	0.30948	0.00000	0.00000

Table S4. Crystallographic information of the R phase of KPF_6 predicted by PBEsol at 0 K and 0 GPa.

Space group	a (Å)	b (Å)	c (Å)	γ (°)
$R\bar{3}$	7.317	7.317	7.094	120.00
Atomic positions				
Atoms	Site	x	y	z
K	3b	0.00000	0.00000	0.50000
P	3a	0.00000	0.00000	0.00000
F	18f	0.79089	0.89837	0.13364